A Stochastic Generator of Global Monthly Wind Energy with Tukey g-and-h Autoregressive Processes

Jaehong Jeong[1], *Yuan Yan*[2], *Stefano Castruccio*[3], *and Marc G. Genton*[2]

Supplementary Material

Section 2

For each spatial location of wind speed after removing the trend, we test significances of skewness and kurtosis over time (Bai and Ng, 2005). The p-values of a significance test for skewness and kurtosis in many spatial locations are smaller than 0.05 as in Figure 1(a) and (b). This indicates a rejection of the Gaussianity null in favor of the non-Gaussian distribution at the usual 5% level. Thus, the first two moments are not sufficient for temporal dependence at least in the modeling of monthly wind speed, and we need to consider the skewness and kurtosis as well.

Department of Mathematics and Statistics, University of Maine, Orono, ME 04469, USA. E-mail: jaehong.jeong@maine.edu.

Statistics Program, King Abdullah University of Science and Technology, Thuwal 23955-6900, Saudi Arabia. E-mail: yuan.yan@kaust.edu.sa, marc.genton@kaust.edu.sa.

Department of Applied and Computational Mathematics and Statistics, 153 Hurley Hall, University of Notre Dame, Notre Dame, IN 46556, USA. E-mail: scastruc@nd.edu.

This publication is based upon work supported by the King Abdullah University of Science and Technology (KAUST) Office of Sponsored Research (OSR) under Award No: OSR-2015-CRG4-2640.

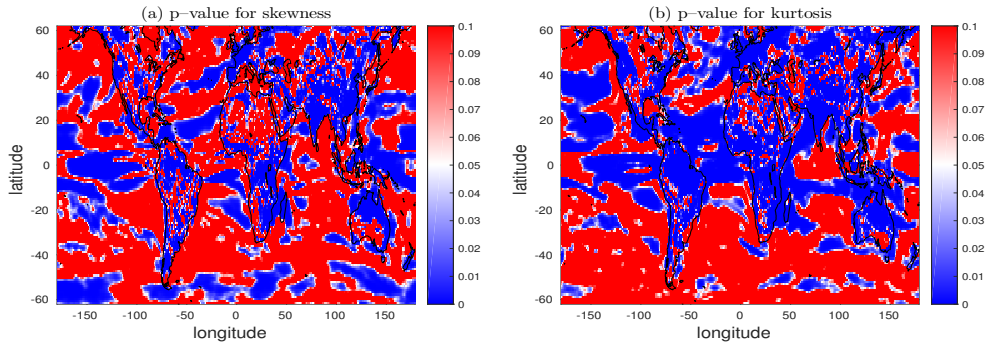

Figure 1: p-values of a significance test for (a) skewness (equals to 0) and (b) kurtosis (equals to 3) over time for one selected ensemble member.

For Gaussianity, the Lilliefors and Jarque-Bera tests are used for testing a null hypothesis that the data comes from the normal distribution (Lilliefors, 1967; Jarque and Bera, 1987). For these tests (Figure 2), there are 15,347 (39.77%) and 23,923 (61.99%) out of 38,592 points where p-value < 0.05, respectively. Many locations show clear evidence of significance for non-Gaussian assumption.

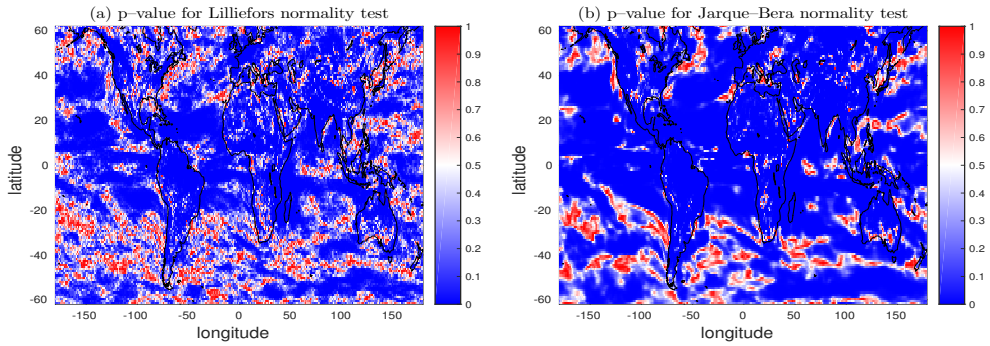

Figure 2: p-values for (a) Lilliefors and (b) Jarque-Bera normality tests.

Section 3.2

Figure 3 shows the p-values for the significance of the first temporal lag of the cross-correlation between innovations one lag apart. Figure 4 maps the estimates of the first three autoregressive coefficients from one randomly selected ensemble member. Figure 5 shows the corresponding p-value for the significance. Figure 6 shows the p-values for the significance of the esitmated g and h in the Tukey random field.

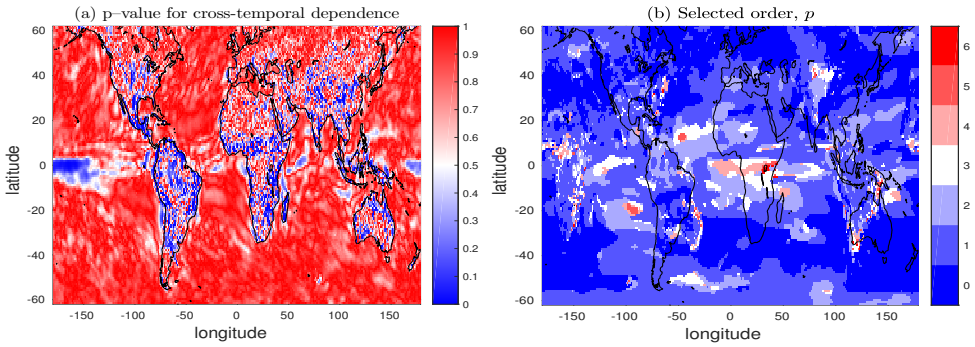

Figure 3: (a) p-values of the first temporal lag of the cross-correlation for the innovations between locations that are one longitudinal lag apart. (b) Plot of the selected order for the TGH-AR(p).

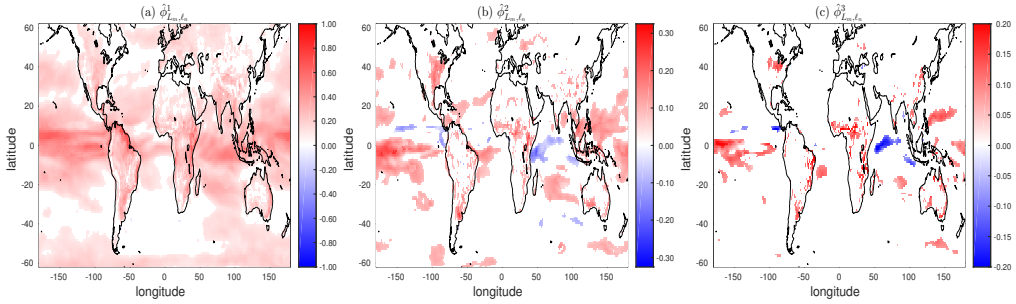

Figure 4: Plot of the first three estimated autoregressive parameters, (a) $\hat{\phi}^1_{L_m,\ell_n}$, (b) $\hat{\phi}^2_{L_m,\ell_n}$, and (c) $\hat{\phi}^3_{L_m,\ell_n}$, from one ensemble member.

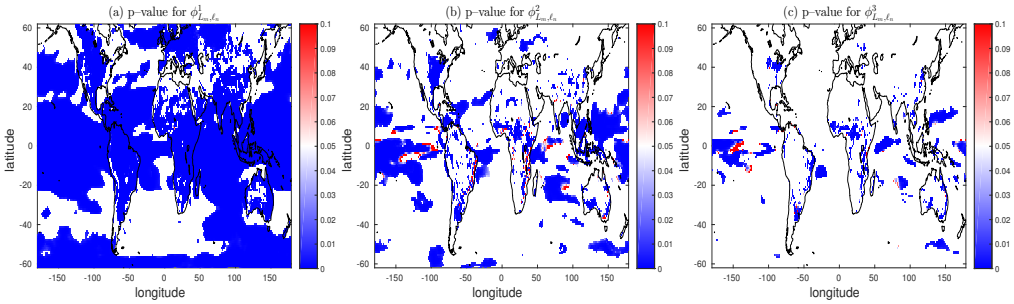

Figure 5: p-values of the first three autoregressive parameters, (a) $\phi^1_{L_m,\ell_n}$, (b) $\phi^2_{L_m,\ell_n}$, and (c) $\phi^3_{L_m,\ell_n}$, from one ensemble member.

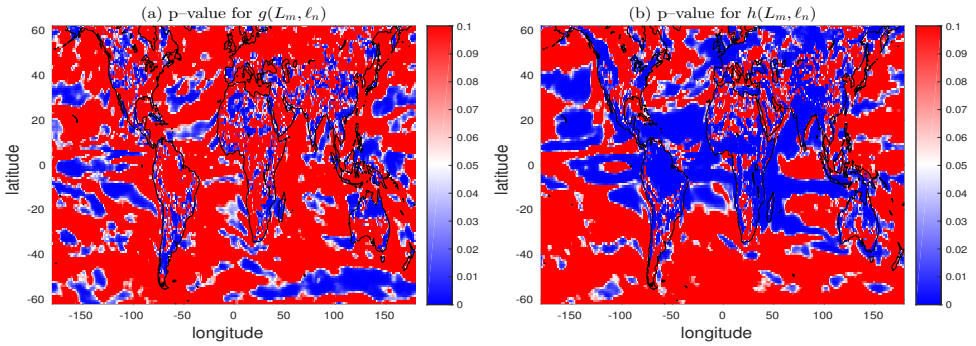

Figure 6: p-values of the Tukey g-and-h transformation parameters, (a) $g(L_m,\ell_n)$ and (b) $h(L_m,\ell_n)$, from one ensemble member.

Section 3.4

$\boldsymbol{\varphi}_{L_m}$ can be written in the following form

$$\boldsymbol{\varphi}_{L_m} = \begin{pmatrix} \varphi_{L_m}(c_1) & \frac{\{1-\varphi_{L_m}(c_1)\}a_{L_m}}{4} & \frac{\{1-\varphi_{L_m}(c_1)\}b_{L_m}}{4} & 0 & \cdots & 0 & 0 & 0 \\ \frac{\{1-\varphi_{L_m}(c_2)\}a_{L_m}}{4} & \varphi_{L_m}(c_2) & \frac{\{1-\varphi_{L_m}(c_2)\}a_{L_m}}{4} & \frac{\{1-\varphi_{L_m}(c_2)\}b_{L_m}}{4} & \cdots & 0 & 0 & 0 \\ \frac{\{1-\varphi_{L_m}(c_3)\}b_{L_m}}{4} & \frac{\{1-\varphi_{L_m}(c_3)\}a_{L_m}}{4} & \varphi_{L_m}(c_3) & \frac{\{1-\varphi_{L_m}(c_3)\}a_{L_m}}{4} & \cdots & 0 & 0 & 0 \\ \vdots & \vdots & \vdots & \vdots & \ddots & \vdots & \vdots & \vdots \\ 0 & 0 & 0 & 0 & \cdots & \frac{\{1-\varphi_{L_m}(c_{N-1})\}a_{L_m}}{4} & \varphi_{L_m}(c_{N-1}) & \frac{\{1-\varphi_{L_m}(c_{N-1})\}a_{L_m}}{4} \\ 0 & 0 & 0 & 0 & \cdots & \frac{\{1-\varphi_{L_m}(c_N)\}b_{L_m}}{4} & \frac{\{1-\varphi_{L_m}(c_N)\}a_{L_m}}{4} & \varphi_{L_m}(c_N) \end{pmatrix}. \quad \text{(S0.1)}$$

Figure 7 shows the parameter estimate for step 3 in the model across the ten sequential time subsamples consisting of the different decades considered. Figure 8 shows similar results for the two-band parameters.

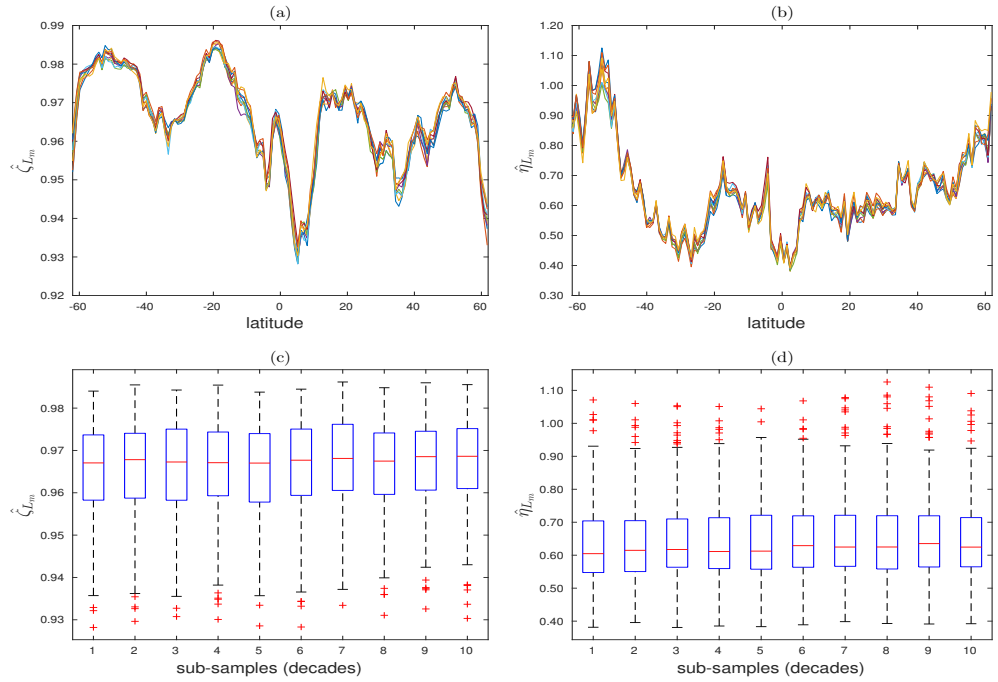

Figure 7: Parameter estimates of (a) ζ_{L_m} and (b) η_{L_m} for 10 sequential sub-samples represented by 10 different colors. Boxplots of estimates of (c) ζ_{L_m} and (d) η_{L_m} across latitudes at each sub-sample.

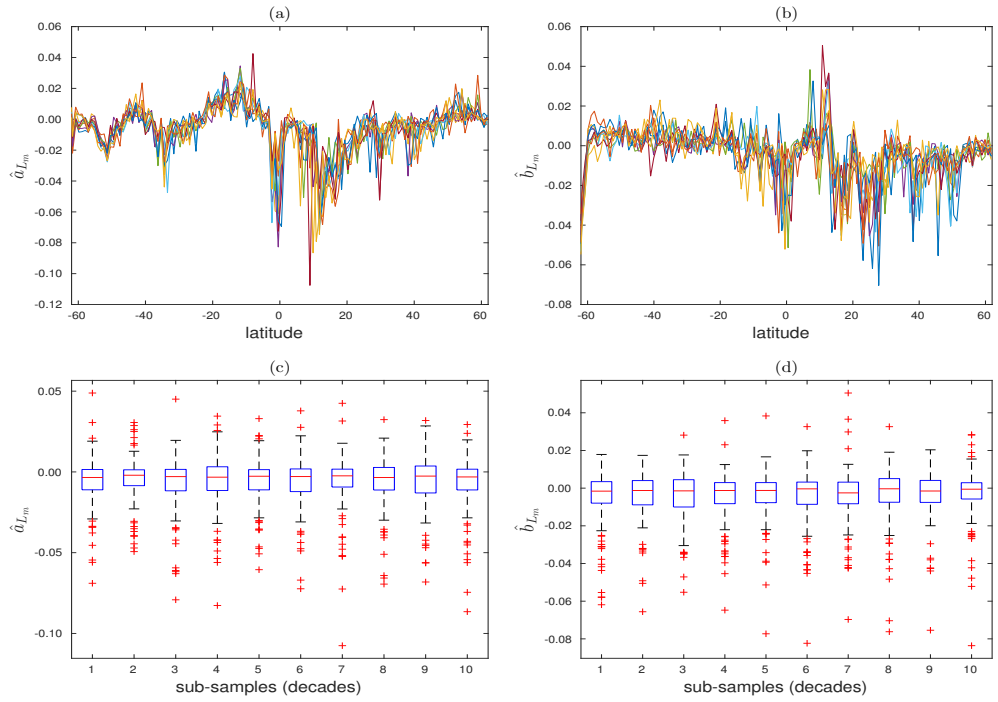

Figure 8: Parameter estimates of (a) a_{L_m} and (b) b_{L_m} for 10 sequential sub-samples. Boxplots of estimates of (c) a_{L_m} and (d) b_{L_m} across latitudes at each sub-sample.

Section 4

For the comparison with our model (T), with a model with no spatial dependence (I), we first focus on a single simulation for May 2020, see Figure 9. While the marginal values simulated by I are still physically coherent (i.e., there are lower winds generally over land), the lack of spatial dependence creates maps which are clearly unphysical, as apparent from the panel (b).

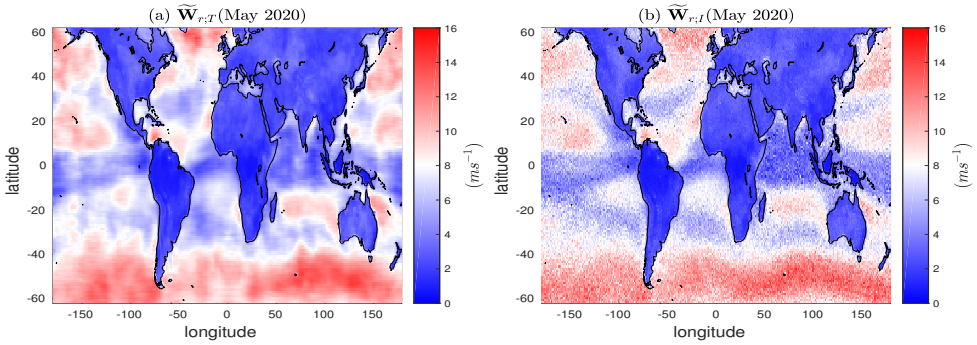

Figure 9: Maps of one realization of wind speeds from (a) T and (b) I runs

For the comparison of T with a model with Gaussian dependence (G), in Figure 10 we showed the empirical estimates of skewness and kurtosis (over time) for one LENS run in panels (a–b) (same as in Figure 1 (e–f) in the main manuscript), compared with the same estimates according to a simulation from the T model (c–d) and G model (e–f). It is apparent that the G model is able to capture neither third nor fourth moment of the distribution, while the T model captures the magnitude and spatial

variability.

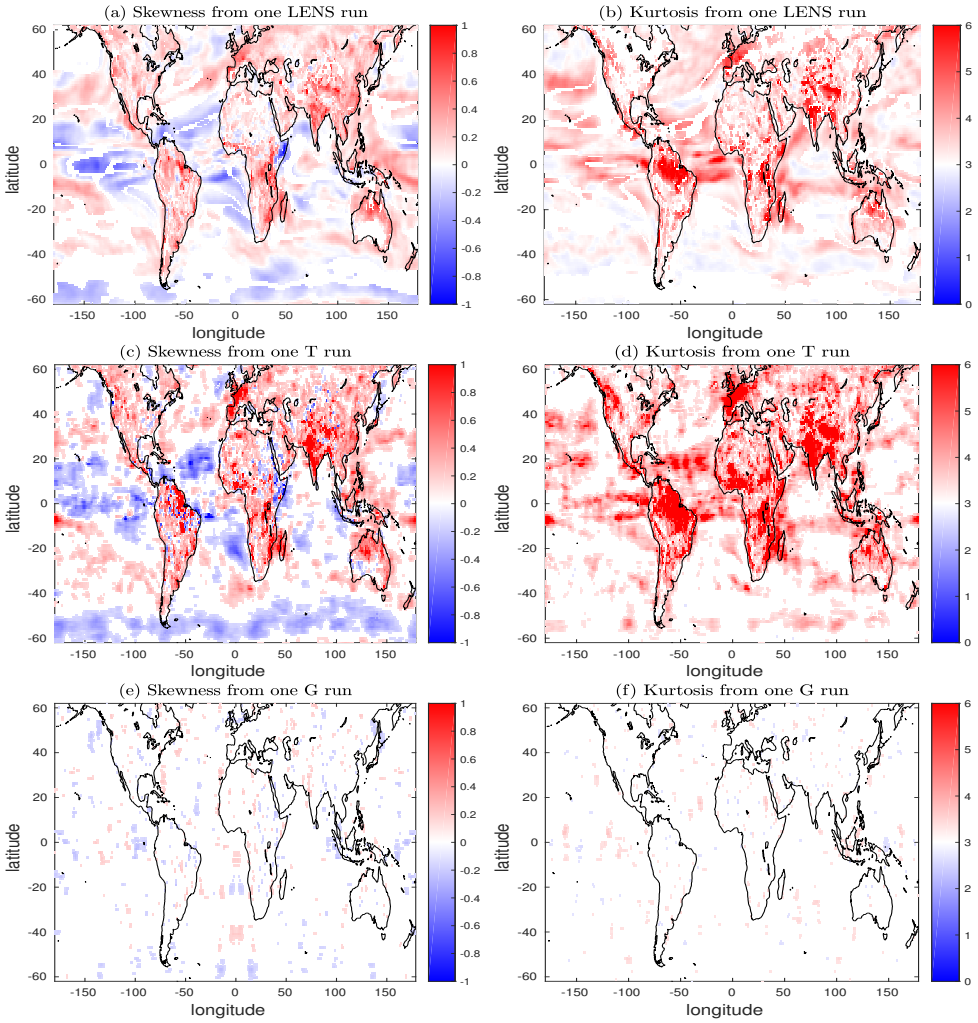

Figure 10: The empirical skewness and kurtosis of residuals after subtracting the trend from one LENS, T, and G runs, respectively. Only for the locations where p-values of a significance test are less than 0.05.

Figure 11 shows a comparison in terms of the fitted contrast variances in a region including South Africa.

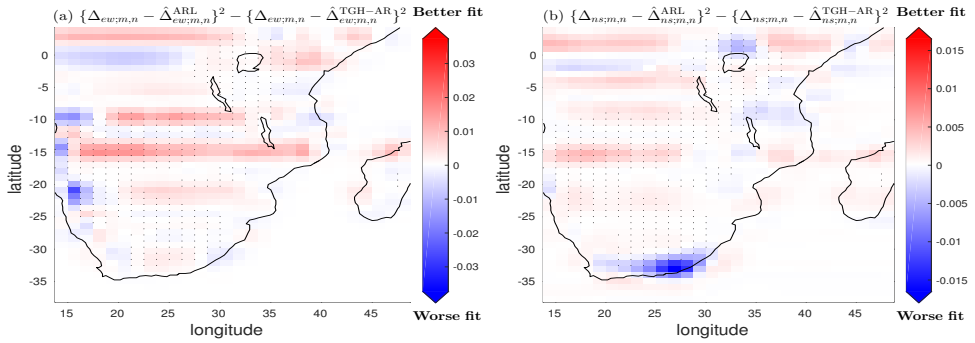

Figure 11: Squared distances of the fitted contrast variances from the empirical contrast variances between two models, ARL and TGH-AR, near Indian ocean: (a) $\{\Delta_{ew;m,n} - \hat{\Delta}^{\mathrm{ARL}}_{ew;m,n}\}^2 - \{\Delta_{ew;m,n} - \hat{\Delta}^{\mathrm{TGH-AR}}_{ew;m,n}\}^2$ and (b) $\{\Delta_{ns;m,n} - \hat{\Delta}^{\mathrm{ARL}}_{ns;m,n}\}^2 - \{\Delta_{ns;m,n} - \hat{\Delta}^{\mathrm{TGH-AR}}_{ns;m,n}\}^2$. Black dots indicate the locations where the surface altitude is larger than 1,000 m.

Section 5

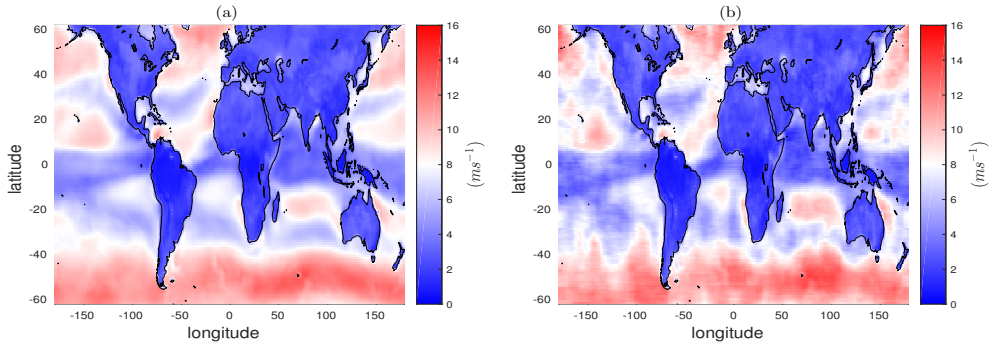

Figure 12: Global maps of (a) the mean from 40 SG runs and (b) one SG run based on the Tukey g-and-h case.

We can measure image quality by computing the structural similarity index (SSIM, (Wang et al., 2004)). Figure 13(a) gives a representation of the computed SSIMs, from Jan 2006 to Dec 2100, for an average of reproduced wind speed across 40 runs based on the Tukey g-and-h and

Gaussian cases using the reference of average wind speed across the 40 LENS runs. In Figure 13(b), we show computed SSIMs for one selected, reproduced wind speed based on different cases using the reference of one selected wind speed from the non-traing set of the remaing 35 LENS runs. In terms of structural similarity, the Tukey g-and-h case has slightly larger values and is more similar to the LENS runs than the Gaussian case. These results are in agreement with the temporal patterns in Figure 16. All LENS and SG runs show similar values of wind speed near the Gulf of Aden as time evolves.

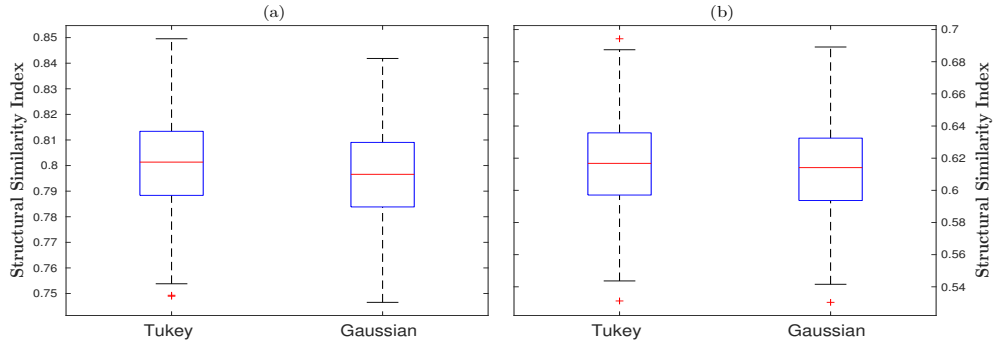

Figure 13: Structural similarity index between the 40 LENS runs and SG runs based on the Tukey g-and-h and Gaussian cases. (a) SSIMs for average from 40 runs and (b) SSIMs for one selected run.

We then compare the empirical skewness and kurtosis from 40 LENS runs with those from each model's 40 SG runs. Figure 14 represents averages of skewness and kurtosis across longitudes and runs from each model. We find that the skewness values obtained from the Tukey g-and-h model are

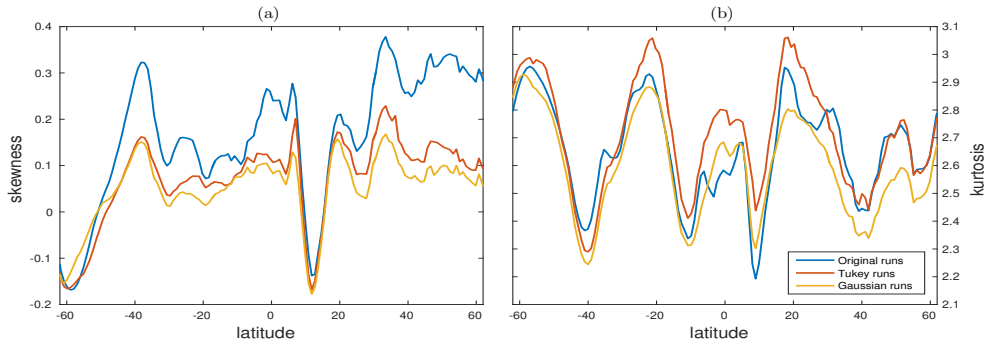

Figure 14: Averages of (a) skewness and (b) kurtosis across longitudes and runs from each model runs (40 LENS runs and 40 SG runs from each model were used). For (b), trimmed mean excluding 10% of outliers.

similar to the empirical values from the climate model than the Gaussian model, while, for several latitudes, it indicates larger kurtosis values than the empirical skewness. Although the empirical kurtosis values are better matched by the Tukey g-and-h case at latitudes $30 \sim 60°$N, we observe that the kurtosis values are much larger than the empirical values near several locations, such as western Europe, western China, Central America, and West Africa.

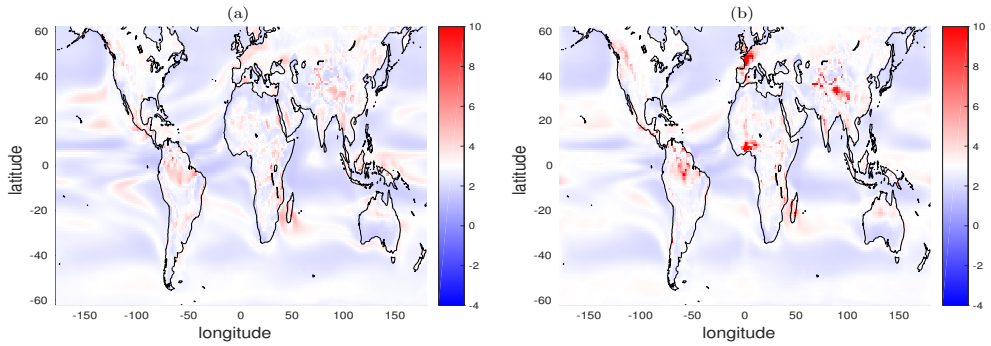

Figure 15: Averages of kurtosis across runs from (a) the LENS and (b) the SG.

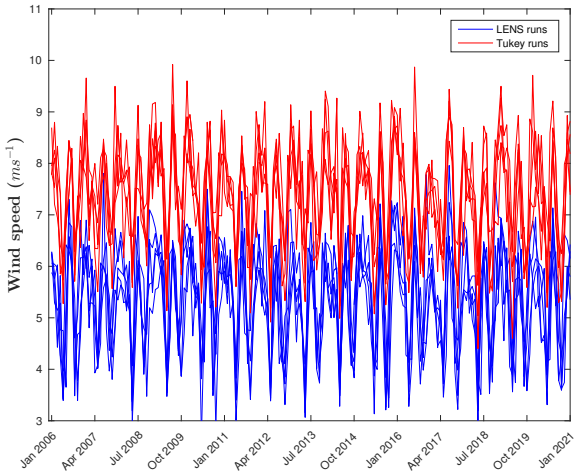

Figure 16: Wind speeds near the Gulf of Aden, from Jan 2006 to Jan 2021, from the traing set of LENS (blue lines) and five SG runs (red lines, offset by $2ms^{-1}$).

Figure 17 shows a comparison with T and I as in the previous Section, same location and months as in Figure 4. The T model clearly follows more closely the ideal 45 degrees line.

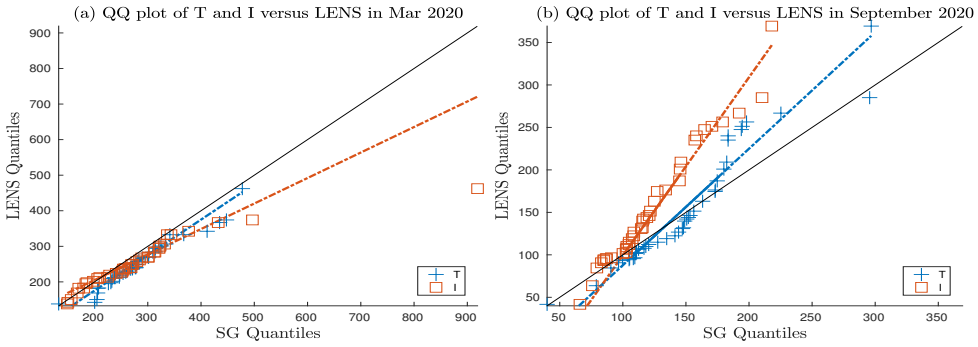

Figure 17: QQ-plots between the WPD values from the LENS runs versus T and I runs in (a) March and (b) September 2020.

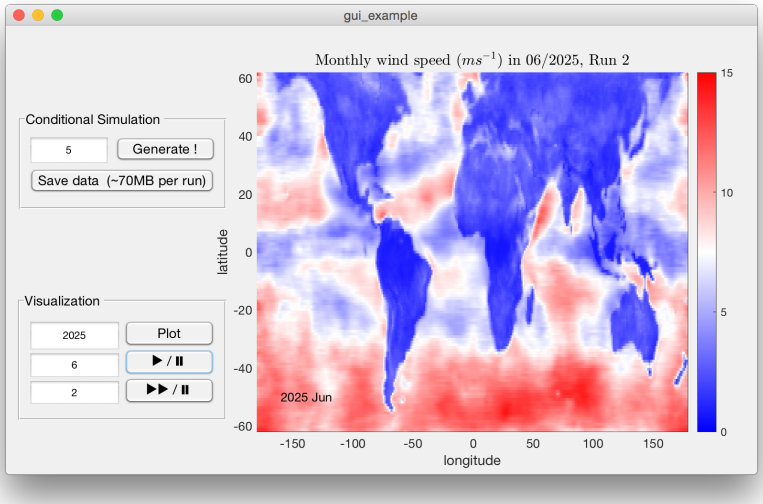

Figure 18: An example of the GUI for the generation of surrogate runs.

Bibliography

Bai, J. and S. Ng (2005). Tests for Skewness, Kurtosis, and Normality for Time Series Data. *Journal of Business & Economic Statistics 23*(1), 49–60.

Jarque, C. M. and A. K. Bera (1987). A Test for Normality of Observations and Regression Residuals. *International Statistical Review/Revue Internationale de Statistique*, 163–172.

Lilliefors, H. W. (1967). On the Kolmogorov-Smirnov Test for Normality with Mean and Variance Unknown. *Journal of the American Statistical Association 62*(318), 399–402.

Wang, Z., A. C. Bovik, H. R. Sheikh, and E. P. Simoncelli (2004). Image Quality Assessment: From Error Visibility to Structural Similarity. *IEEE Transactions on Image Processing 13*(4), 600–612.